PAPER

Hollow SnO$_2$/α-Fe$_2$O$_3$ spheres with a double-shell structure for gas sensors†

Peng Sun,[a] Xin Zhou,[a] Chen Wang,[a] Kengo Shimanoe,[b] Geyu Lu*[a] and Noboru Yamazoe[b]

Double-shell SnO$_2$/α-Fe$_2$O$_3$ hollow composites were synthesized by a low-cost and environmentally friendly hydrothermal strategy. Various techniques were employed for the characterization of the structure and morphology of hybrid nanostructures. The results revealed that the α-Fe$_2$O$_3$ nanorods grew epitaxially on the surface of hollow SnO$_2$ spheres, which were composed of primary nano-sized particles. The diameter of the α-Fe$_2$O$_3$ nanorods was about 10 nm, and the thickness of the SnO$_2$ spherical shell was about 100 nm. In order to explore the formation mechanism of the composites, the structure features of the double-shell structural SnO$_2$/α-Fe$_2$O$_3$ hollow composites at different reaction stages were investigated. The ethanol sensing properties of the pure SnO$_2$ and SnO$_2$/α-Fe$_2$O$_3$ composites were tested. It was found that such double-shell composites exhibited enhanced ethanol sensing properties compared with the single-component SnO$_2$ hollow spheres. For example, at an ethanol concentration of 100 ppm, the response of the SnO$_2$/α-Fe$_2$O$_3$ composites was about 16, which was about 2 times higher than that of the primary SnO$_2$ nanostructures. The response time of the sensor to 10 ppm ethanol was about 1 s at the operating temperature of 250 °C.

1. Introduction

In recent years, gas sensors have been the focus of worldwide research owing to their applications in detecting pollutant, toxic and combustible gases.[1–3] It is well known that high sensitivity, rapid response, and excellent selectivity are the three most important parameters in designing oxide semiconductor gas sensors. Therefore, developing new sensor strategies for ever increasing sensitivity, improvement selectivity, and reduction of cost represents one of the major scientific challenges.[4–6] A critical element in the pursuit of this quest is discovery of efficient and cost-effective sensing materials. Indeed, it has been demonstrated that materials with high surface area are advantageous for obtaining a high sensitivity in sensing applications.[7,8] Due to well-defined interior voids, high specific surface area, low density, and good surface permeability, hollow nanostructures have attracted growing interest in recent years and should deserve more attention on controllable synthesis due to their wide applications.[9–12] Not until now the synthesis often depends on complicated templating approaches,[13] in which hard (*e.g.*, monodispersed silica and carbon spheres) or soft sacrificial templates (*e.g.*, supramolecular assemblies of surfactant and polymer) are used to create a hollow structure. However, template contamination mostly decreases the activity of synthesized materials and the synthetic procedure is tedious and of high cost. Recently, a number of template-free methods for preparing hollow inorganic microstructures and nanostructures have been developed.[14–17] Despite the intense effort that has been made, it is still highly desirable to develop facile, solution-based, and template free self-assembly methods for the preparation of hollow structures.

As important functional materials, SnO$_2$ and α-Fe$_2$O$_3$ with band gaps of ~3.6 eV and ~2.2 eV, respectively, have been intensively investigated due to their unique properties and great potential applications. Recently, many studies have demonstrated that the performance of SnO$_2$ or Fe$_2$O$_3$ in gas sensing, photocatalytic degradation and lithium ion batteries can be significantly improved by formation of SnO$_2$/Fe$_2$O$_3$ composites.[18–22] Therefore, various SnO$_2$/Fe$_2$O$_3$ composites with hierarchical architectures have been prepared. It is found that the performances of these composites are closely related to their structure. For this reason, design and synthesis of SnO$_2$/Fe$_2$O$_3$ composites with novel architectures still have important scientific and practical significance. In this paper, we successfully prepared double-shell SnO$_2$/α-Fe$_2$O$_3$ hollow composites by two-step hydrothermal reactions. First, hollow SnO$_2$ spheres composed of nanoparticles were synthesized. Subsequently, one-dimensional (1D) α-Fe$_2$O$_3$ nanorods were assembled epitaxially on the surface of SnO$_2$ hollow spheres by a

[a]*State Key Laboratory on Integrated Optoelectronics, College of Electronic Science and Engineering, Jilin University, Changchun 130012, People's Republic of China. E-mail: lugy@jlu.edu.cn; Fax: +86 431 85167808; Tel: +86 431 85167808*

[b]*Department of Energy and Material Sciences, Faculty of Engineering Sciences, Kyushu University, Kasuga-shi, Fukuoka 816-8580, Japan*

† Electronic supplementary information (ESI) available. See DOI: 10.1039/c3ta13707d

hydrothermal process. The structure features of the double-shell structural SnO_2/α-Fe_2O_3 composites at various reaction stages were investigated aiming to explore the formation mechanism of such a novel structure. In order to demonstrate the potential applications, the resulting composite was used to fabricate a gas sensor. It was found that the gas sensor based on as-prepared SnO_2/α-Fe_2O_3 double-shell structural composites showed a high response to ethanol at 250 °C, superior to the pure SnO_2 hollow nanostructures. The enhanced performance may be attributed to the novel structure as well as the change of the heterojunction barrier at the different gas atmosphere.

2. Experimental section

2.1 Synthesis and characterization

Tin(II) oxalate (SnC_2O_4), $FeCl_3\cdot 6H_2O$, and $Na_2SO_4\cdot 10H_2O$ were purchased from Sinopharm Chemical Reagent Co., Ltd. SnO_2 hollow nanostructures were synthesized *via* a facile hydrothermal process. Briefly, 0.45 mL of concentrated hydrochloric acid (concentration: 36–38%) was added to an ethanol–deionized water (volume ratio: 10 : 1) solution with vigorous stirring under ambient conditions before 0.175 g of SnC_2O_4 was introduced. Then the mixture was ultrasonicated for 30 min. The resulting solution was transferred into a Teflon-lined stainless-steel autoclave and kept at 200 °C for 24 h. The autoclave was cooled down naturally after the reaction. The precipitate was collected and washed by centrifugation several times before drying at 80 °C for 12 h. The obtained product was fired at 500 °C for 2 h using a muffle furnace.

The double-shell SnO_2/α-Fe_2O_3 hollow composites were prepared by a surfactant-free hydrothermal strategy. Typically, 0.05 g of the above SnO_2 powder was dispersed in 16 mL of deionized water under magnetic stirring vigorously. Then, 0.216 g of $FeCl_3\cdot 6H_2O$ and 0.258 g of $Na_2SO_4\cdot 10H_2O$ were added into the above solution, respectively. After stirring, the formed suspension was transferred into a Teflon-lined stainless-steel autoclave and heated at 120 °C for 10 h. The resulting product was collected *via* centrifugation and washed with deionized water and absolute ethanol several times, and dried at 80 °C. Finally, the hollow SnO_2/α-Fe_2O_3 composites were obtained by annealing the as-prepared precipitates in air at 500 °C for 2 h. A red powder was obtained, which was collected for further analysis and characterization.

X-ray power diffraction (XRD) analysis was conducted on a Rigaku TTRIII X-ray diffractometer with Cu Kα 1 radiation ($\lambda = 1.5406$ Å) in the range of 20–80°. Field emission scanning electron microscopy (FESEM) images were recorded on a JEOL JSM-7500F microscope operating at 15 kV. Transmission electron microscopy (TEM) and high-resolution transmission electron microscopy (HRTEM) images were obtained on a JEOL JEM-3010 microscope operating at 200 kV, respectively. The energy dispersive X-ray spectrometry (EDS) result was measured by the TEM attachment. Brunauer–Emmett–Teller (BET) equation based on the nitrogen adsorption isotherm was obtained with a Micromeritics Gemini VII apparatus (surface area and porosity system).
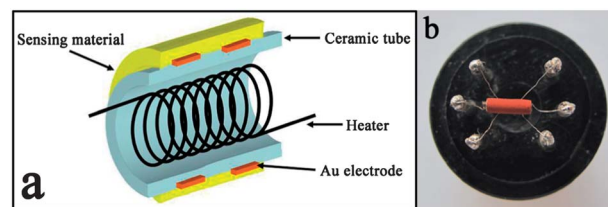

Fig. 1 (a) Schematic diagram of the sensor. (b) Photograph of the completed sensor.

2.2 Fabrication and measurement of gas sensors

Gas sensors were fabricated as follows: the prepared products were mixed with deionized water to form paste, and then coated onto the outside of an alumina tube (4 mm in length, 1.2 mm in external diameter, and 0.8 mm in internal diameter, attached with a pair of gold electrodes) by a small brush to form a thick film. The Ni–Cr alloy coil heater was inserted into the alumina tube. The operating temperature was controlled by adjusting the heating current, which flowed through the heater. A schematic diagram of the as-fabricated sensor and a photograph of the sensor on the socket are shown in Fig 1. The details of the sensor fabrication and the testing process were described in our previous studies.[23,24] The gas response behavior of the sensor was investigated using a static system under laboratory conditions (40 RH%, 23 °C). The test gases were injected into a closed chamber by using a microinjector. The gas response of the sensor was defined as the ratio of the resistance of the sensor in air (R_a) to that in tested gases (R_g). The response time and recovery time were defined as the time taken by the sensor to achieve 90% of the total resistance change after the sensor was exposed to the tested gas and air, respectively.

3. Results and discussion

3.1 Structural and morphological characteristics

The crystal structure and phase purity of the final product were identified by powder X-ray diffraction (XRD). Fig. 2 reveals the overall crystal structure and phase purity of the two as-prepared samples: pristine SnO_2 hollow spheres and hierarchical double-shell SnO_2/α-Fe_2O_3 nanostructures, respectively. All the diffraction peaks for pure SnO_2 matched well with those of standard XRD patterns of the tetragonal rutile structure of SnO_2 with lattice constants of $a = 4.738$ Å and $c = 3.187$ Å. which agreed well with the reported values from the Joint Committee on Powder Diffraction Standards card (JCPDS, 41-1445). Using the Scherrer equation ($D = 0.89\lambda/\beta \cos\theta$ where D is the crystallite size, λ the wavelength of X-ray, β the line broadening at full width half-maximum, and θ the Bragg diffraction angle of the peak) to calculate the crystallite size for the as-synthesized product indicated a mean crystallite size of about 18 nm. For the composites, the crystal phases were the mixed oxide of SnO_2 and α-Fe_2O_3, most of the diffraction peaks could be indexed to the tetragonal rutile structure of SnO_2. The residual peaks were indexed to the rhombohedral structure of α-Fe_2O_3 with space group $R\bar{3}c$ (no. 167) and lattice parameters of $a = 5.035$ Å

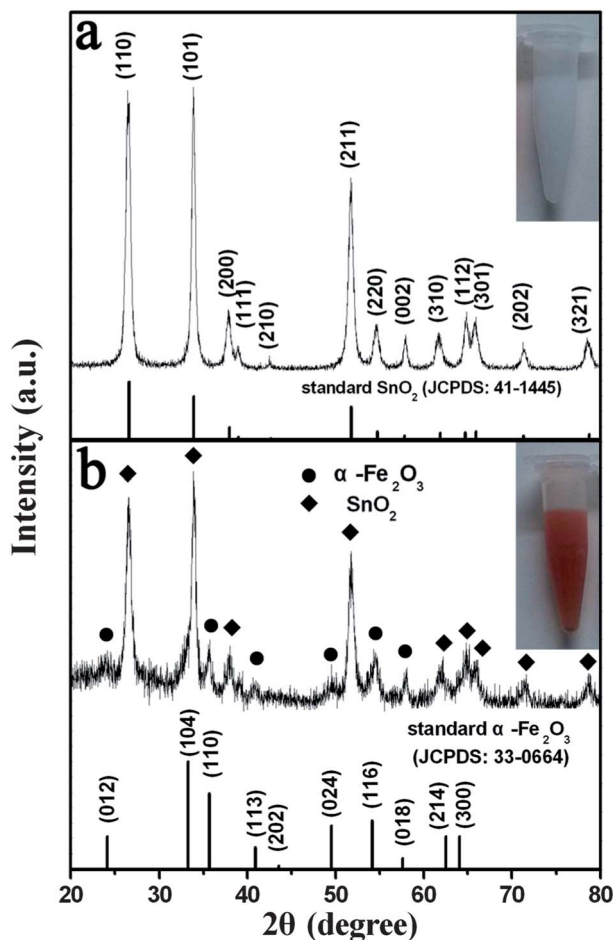**Fig. 2** XRD patterns of the as-prepared SnO_2 hollow spheres (a) and double-shell structural composites (b).

Fig. 3 (a) Typical FESEM image of SnO_2 spheres. (b and c) High-magnification FESEM images. (d and e) Typical TEM images of SnO_2 spheres. (f) HRTEM image.

and $c = 13.75$ Å, which was consistent with the standard date file 33-0664. No other diffraction peaks corresponding to impurities were observed, which indicated that the product had a high purity.

A panoramic FESEM image of the as-prepared pristine SnO_2 is shown in Fig. 3a, from which a number of uniform and monodisperse spherical particles were clearly observed. No other morphologies could be detected, indicating a high yield of these spheres. It can be observed from the enlarged FESEM image of Fig. 3b that the diameter of the obtained SnO_2 sphere was about 400 nm. Apparently, the rough surface of the spherical structure was exhibited. A broken SnO_2 sphere is shown in Fig. 3c, which clearly demonstrated that the sphere possessed a hollow structure. Moreover, the SnO_2 sphere was enclosed entirely by aggregated SnO_2 nanoparticles with the average size of about 20 nm. The typical transmission electron microscopy (TEM) images in Fig. 3d and e reveal the hollow nature of the product. The TEM images show that the hollow spheres were surrounded by small nanoparticles, which had an average size of about 20 nm, in accordance with SEM results, while the shell thickness was around 100 nm. Fig. 3f shows a high-resolution TEM (HRTEM) image of SnO_2 nanoparticles on the sphere surface, which confirmed that the as-prepared SnO_2
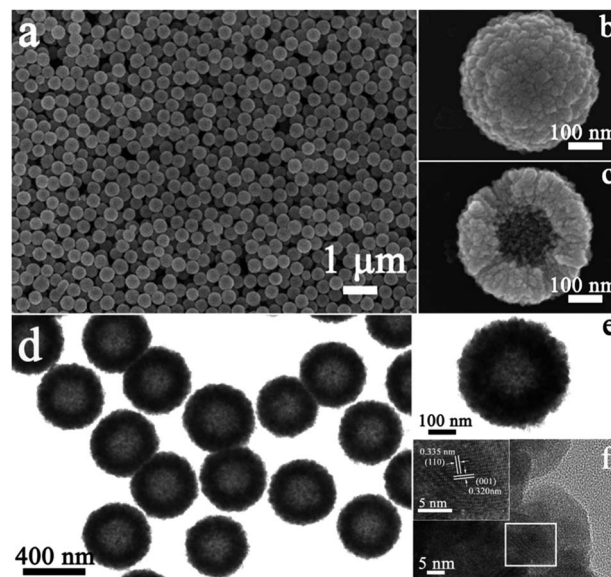
nanoparticles were single-crystalline. The marked spacings of about 0.335 and 0.32 nm for the lattice fringes agreed well with the (110) and (001) planes in a tetragonal rutile phase.[25] The BET surface area of as-prepared SnO_2 hollow spheres was calculated to be 68.8 m^2 g^{-1} (see ESI, Fig. S1a†).

After applying the growth solution of α-Fe_2O_3 nanorods, the initially hollow SnO_2 spheres branched out, forming double-shell SnO_2/α-Fe_2O_3 hollow composites. Fig. 4a shows a typical low-magnification SEM image of the composites, it is composed of a large number of well-dispersed spherical particles. The average diameter of the spheres was about 600 nm (Fig. 4b). The high-magnification FESEM image (Fig. 4c) displays the detailed morphological information of such a composite. It can be seen that the surface of the sphere bristled with nanorods, and the average diameter of nanorods was about 10 nm. When observed under a transmission electron microscope (TEM), a distinct hollow interior could be clearly identified (Fig. 4d). Closer TEM observation of a single sphere (Fig. 4e) confirms that these hybrid spheres have a clear double-shell structure. The inner shell could be identified as a hollow SnO_2 sphere, and it appeared as a bulky dark region merged with the outer shell, indicating that the inner shell was probably encapsulated by SnO_2 nanoparticles, in keeping with the SEM results (Fig. 3c and e). The outer shell of the hollow sphere composed of α-Fe_2O_3 nanorods with the average length of about 100 nm. Fig. 4f shows a HRTEM image of α-Fe_2O_3 nanorods, which indicated that the nanorods were single-crystalline. The lattice fringe spacing was observed to be 0.265 nm, corresponding to the (0$\bar{1}$4) plane of α-Fe_2O_3.[26] The EDS analysis (Fig. S2†) reveals that the composition of hierarchical composites consisted of Sn, Fe and O elements. Fig. 4g shows the scanning TEM (STEM) image of a single sphere. The TEM elemental mapping was conducted to clearly identify the spatial distributions of Sn and Fe in the

1304 | *J. Mater. Chem. A*, 2014, **2**, 1302–1308

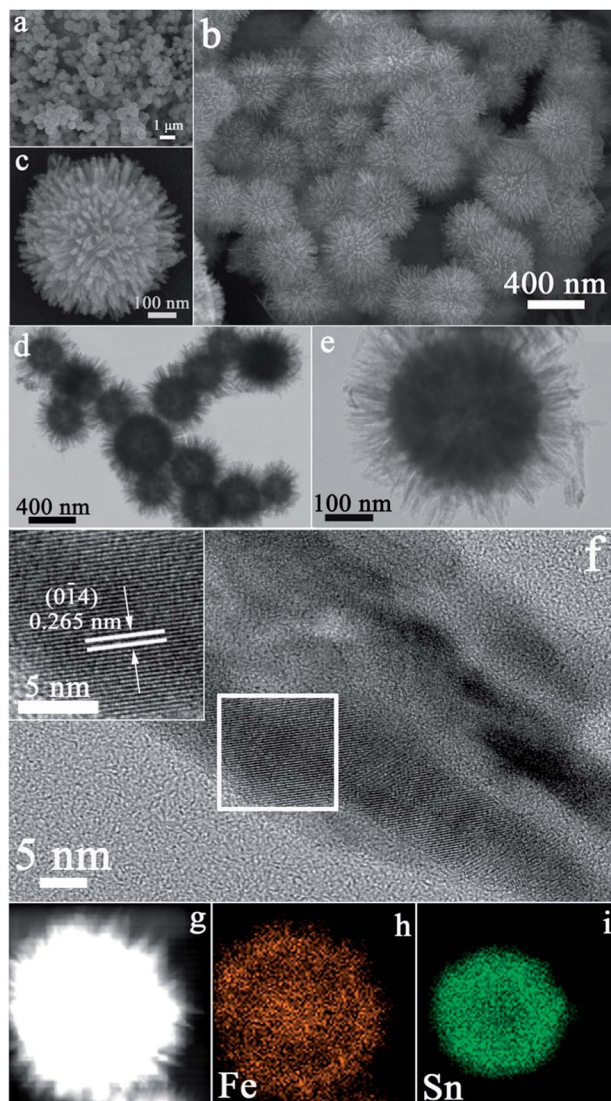This journal is © The Royal Society of Chemistry 2014

Fig. 4 (a–c) Typical FESEM images of hollow double-shell composites. (d and e) Typical TEM images of composites. (f) HRTEM image. (g–i) The scanning TEM (STEM) image and the corresponding elemental mapping images.
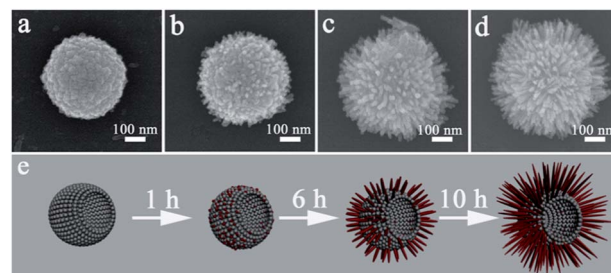

Fig. 5 SEM images of the products at various reaction stages after heat treatment: (a) having reaction for 0 h, (b) having reaction for 1 h, (c) having reaction for 6 h, and (d) having reaction for 10 h. (e) Schematic of the formation process of the composite.

observed (Fig. 5b). These small α-Fe_2O_3 (Fig. S3†) nanoparticles displayed a thorn-like shape, indicating the tendency of anisotropic growth. When the reaction proceeded to 6 h, the as-formed thorn-like nanoparticles elongated, evolving to the rudiments of nanorods (Fig. 5c). As the reaction prolonged to 10 h, the length and diameter of nanorods increased, and the product exhibited an urchin-like morphology (Fig. 5d). The detailed characteristics of the sample were described previously. On the basis of the results stated above, the formation process of the double-shell structural SnO_2/α-Fe_2O_3 composites from primary SnO_2 hollow spheres in the hydrothermal system is proposed, as illustrated schematically in Fig. 5e. Initially, the FeOOH nuclei would form on the surfaces of SnO_2 hollow spheres through a hydrolyzation of $FeCl_3$. When crystals nucleated from the solution, the thorn-like nanoparticles would be formed owing to the growth of crystals. Secondly, these nanoparticles grew into aligned nanorods with increasing reaction time, leading to nanorods surrounding the SnO_2 spheres. The basic theory and conditions for such an anisotropic growth have been elaborated in previous studies.[27,28] As the reaction proceeded further, the length and diameter of nanorods increased to form a spherical shell. Finally, SnO_2/FeOOH topologically transformed into SnO_2/α-Fe_2O_3 double-shell structural composites induced by the thermal annealing. The detailed mechanism for the formation of the novel double-shell structures is still under investigation by our group. Here is a hypothesis that agreed well with the observations of electron microscopy.

3.2 Sensing properties

In order to demonstrate the potential application, gas sensors based on as-synthesized SnO_2/α-Fe_2O_3 double-shell structural composites and hollow SnO_2 spheres were fabricated and their gas sensing performances were investigated. Fig. 6a displays the response of two sensors to 100 ppm ethanol at operating temperature from 150 to 300 °C. It is obvious that the responses of the tested sensors varied with the operating temperature. It is well known that the increase of operating temperature would facilitate the chemical reaction, which will lead to the increase of response to ethanol. However, further increase in temperature resulted in the decrease of response. The reason was attributed to the low utilization rate of the
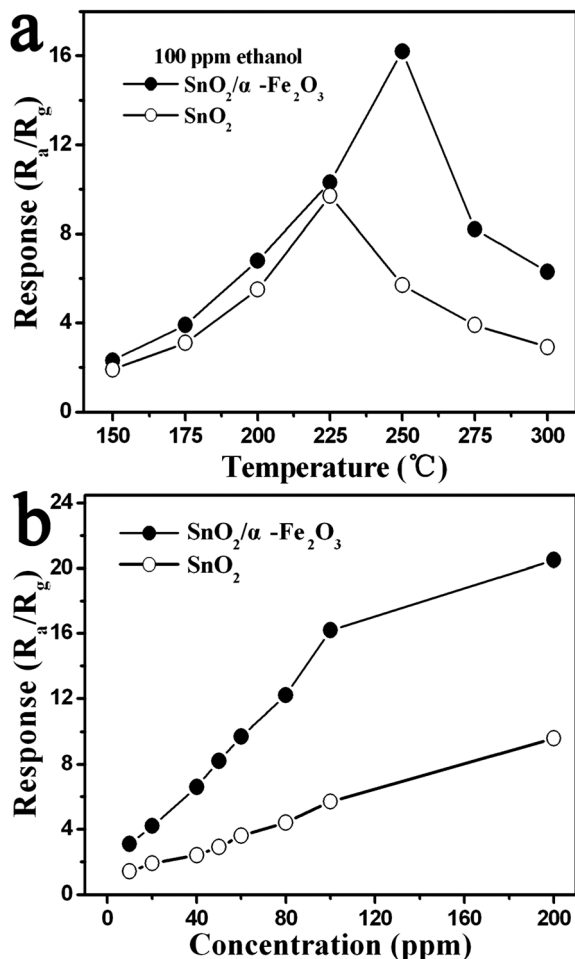
double-shell hollow structure (as shown in Fig. 4h and i). In the inner shell region, the signals of Sn were strongly detected, while the Fe signals were barely visible. In contrast, the Fe signals were dominant in the outer shell region, while the Sn signals were nearly absent. The BET surface area of double-shell SnO_2/α-Fe_2O_3 hollow composites was about 70.6 m^2 g^{-1} (Fig. S1b†).

In order to have a closer inspection of the evolution processes of α-Fe_2O_3 nanorods, a series of time-dependent experiments were carried out. Fig. 5a–d and S3 (see ESI†) show the SEM images and XRD patterns of the products obtained from various reaction stages after heat treatment, indicating the morphological and structural transformation from hollow SnO_2 spheres to SnO_2/α-Fe_2O_3 double-shell structural composites. For the sample that reacted for 1 h, nanoparticles of ~5 nm size nucleated on the surface of the hollow SnO_2 spheres were

This journal is © The Royal Society of Chemistry 2014

J. Mater. Chem. A, 2014, 2, 1302–1308 | 1305

Fig. 6 (a) Response of pure SnO_2 and hollow double-shell structural composites *versus* operating temperature to 100 ppm ethanol. (b) Response of pure SnO_2 and hollow SnO_2/α-Fe_2O_3 composites at 250 °C *versus* ethanol concentrations.

sensing layer because the gas (ethanol) was consumed at the surface of the sensing layer, leading to reduction of the penetration depth of the target gas. Thus, the change in resistance would be decreased. Namely, the sensitivity would be reduced. For pure SnO_2 spheres, the maximum value of response obtained was 9.7 at 225 °C. In contrast the double-shell structural SnO_2/α-Fe_2O_3 composites exhibited a rapid increase of response. At the operating temperature of 250 °C, the response reached the maximum value of 16.2 based on several repeated sensors, which was almost two times higher than that of the obtained response (about 5.7) of the pure SnO_2 nanostructures at the same operating temperature. Fig. 6b shows the response of double-shell composites and pure SnO_2 nanostructures *versus* the concentration of C_2H_5OH at 250 °C. Similar to pure SnO_2 hollow spheres, the response of composites increased with increase in the concentration of ethanol. It was obvious that the sensor based on hollow SnO_2/α-Fe_2O_3 composites displayed quite enhanced response. Moreover, the increase in the responses depended near linearly on the gas concentrations in the range from 10 to 100 ppm for the two sensors.

Fig. 7a shows a bar graph of the responses of the sensor based on as-prepared hollow SnO_2/α-Fe_2O_3 spheres to a variety of gases, such as ethanol, acetone, toluene, *etc.* All of the gases were tested at an operating temperature of 250 °C with a concentration of 10 ppm. The results indicated that the sensor showed selectivity toward ethanol as opposed to any other gas. The dynamic response characteristics of the hollow double-shell composites towards different reducing gases were investigated. Fig. 7b exhibits the response of hollow composites to 10 ppm ethanol, acetone, and toluene at 250 °C, respectively. The almost square response shape observed indicates that the sensor first responded rapidly to test gases and achieved a near steady state.[29] Then the resistance of the sensor changed slowly due to analyte gases diffusing through the material and occupying the remaining surface reaction sites. When the sensor was exposed to air, the resistance returned to near baseline level. The four reversible cycles of the response curve indicated a stable and repeatable characteristic (ESI, Fig. S4†). The time of response was within 1, 6 and 7 s for ethanol, acetone, and toluene, respectively. After exposure to air, the time of recovery was 14, 23 and 32 s for ethanol, acetone, and toluene, respectively.

The enhanced performance observed here is likely to be the result of two factors. First, the hollow SnO_2/α-Fe_2O_3 composites have a porous structure and high surface area. This means that
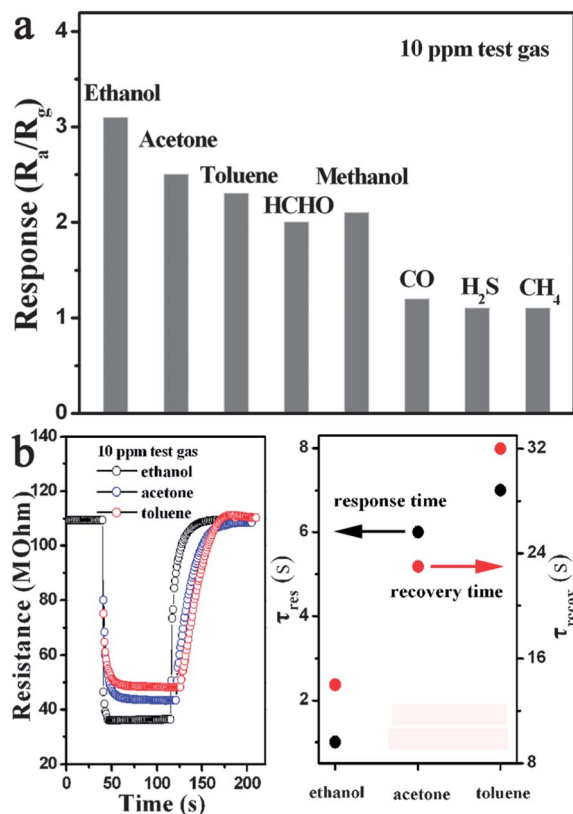

Fig. 7 (a) Responses of the sensor using hollow SnO_2/α-Fe_2O_3 spheres to various gases. (b) Response transients of the sensor based on hollow SnO_2/α-Fe_2O_3 double-shell composites to 10 ppm ethanol, acetone, and toluene at 250 °C.

1306 | *J. Mater. Chem. A*, 2014, **2**, 1302–1308
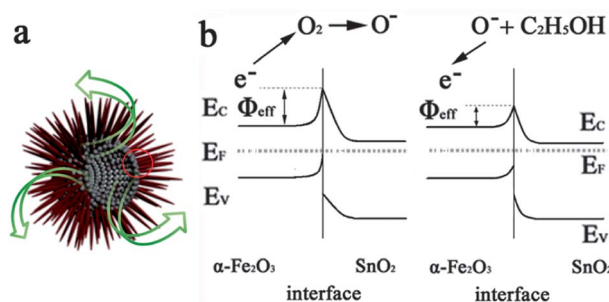
This journal is © The Royal Society of Chemistry 2014

Fig. 8 Schematic diagrams (a) illustrating the plausible reason of fast response and recovery. (b) The energy band structure of the SnO$_2$/α-Fe$_2$O$_3$ heterostructures in air and ethanol.

the amount of oxygen that can be absorbed and ionized is increased.[30] Simultaneously, the diffusion of the test gas (ethanol) can be facilitated and the kinetics of the reaction of the test gas with surface-adsorbed oxygen species will be improved (Fig. 8a). Therefore, a high response and short response time were obtained. Second, according to the theory of semiconductor heterojunction, the energy band structure of the SnO$_2$/α-Fe$_2$O$_3$ heterojunction can be schematically depicted in Fig. 8b, where Φ_{eff} is the effective barrier height.[31] At the high temperature region, the conductivity (G) of the heterostructures under different gas atmospheres can be given by[31]

$$G = G_0 \exp(-q\Phi_{eff}/k_B T) \qquad (1)$$

where q is the charge of an electron, k_B is Boltzmann's constant, and T is the absolute temperature. In this equation, G_0 can be considered as a constant parameter. The electrons in conduction bands of α-Fe$_2$O$_3$ and SnO$_2$ are trapped in the ionized oxygen species in air, which will lead to the increase of Φ_{eff}, as shown in Fig. 8b. In this case, the conductivity of the heterostructures is very low due to the higher barrier potential. However, on exposure to reducing gases such as ethanol and acetone, surface reaction between the oxygen species and gas molecules can occur,[32–34] leading to the release of electrons trapped in the ionized oxygen species back into the conduction bands of α-Fe$_2$O$_3$ and SnO$_2$, thereby lowering the height of the barrier potential at their interfaces, as shown in Fig. 8b. Consequently, the conductivity of the heterostructures will be greatly increased, which results in high response.

4. Conclusions

In summary, a simple solution route was successfully used to prepare hollow SnO$_2$/α-Fe$_2$O$_3$ double-shell structural composites. The as-synthesized sample consists of α-Fe$_2$O$_3$ nanorods and SnO$_2$ hollow nanospheres with a diameter of 400 nm. The structure features of the composites at various reaction stages were investigated in order to explore the formation mechanism of such a novel structure. The obtained product was utilized in sensor devices and their gas sensing properties were examined. It was found that the device based on as-prepared SnO$_2$/α-Fe$_2$O$_3$ double-shell structural composites showed a high response to ethanol at 250 °C, superior to the pure SnO$_2$ hollow

nanostructures. The reason for performance improvement has been discussed.

Notes and references

1 J. Kong, N. R. Franklin, C. Zhou, M. G. Chapline, S. Peng, K. Cho and H. Dai, *Science*, 2000, **287**, 622–625.

2 C. Hagleitner, A. Hierlemann, D. Lauge, A. Kimmer, N. Kerness, O. Brand and H. Baltes, *Nature*, 2001, **414**, 293–296.

3 Y. Cui, Q. Q. Wie, H. K. Park and C. M. Lieber, *Science*, 2001, **293**, 1289–1292.

4 (a) F. H. Ramirez, J. D. Prades, A. Hackner, T. Fischer, G. Mueller, S. Mathar and J. R. Morante, *Nanoscale*, 2011, **3**, 630–634; (b) S. Cui, S. Mao, G. Lu and J. Chen, *J. Phys. Chem. Lett.*, 2013, **4**, 2441–2454; (c) Y. H. Lin, Y. C. Hsueh, P. S. Lee, C. C. Wang, J. M. Wu, T. P. Perng and H. C. Shih, *J. Mater. Chem.*, 2011, **21**, 10552–10558.

5 (a) H. N. Hieu, N. M. Vuong, H. Jong, D. M. Jang, D. Kim, H. Kim and S. K. Hong, *J. Mater. Chem.*, 2012, **22**, 1127–1134; (b) C. Li, D. H. Zhang, X. L. Liu, S. Han, T. Tang, J. Han and C. W. Zhou, *Appl. Phys. Lett.*, 2003, **82**, 1613–1615.

6 (a) S. Mao, S. Cui, G. Lu, K. Yu, Z. Wen and J. Chen, *J. Mater. Chem.*, 2012, **22**, 11009–11013; (b) M. Law, H. Kind, B. Messer, F. Kim and P. D. Yang, *Angew. Chem., Int. Ed.*, 2002, **41**, 2405–2408.

7 (a) J. H. Lee, *Sens. Actuators, B*, 2009, **140**, 319–336; (b) G. Sakai, N. Matsunaga, K. Shimanoe and N. Yamazoe, *Sens. Actuators, B*, 2001, **80**, 125–131.

8 (a) K. I. Choi, H. R. Kim and J. H. Lee, *Sens. Actuators, B*, 2009, **138**, 497–503; (b) S. Mao, S. Cui, K. Yu, Z. Wen, G. Lu and J. Chen, *Nanoscale*, 2012, **4**, 1275–1279.

9 (a) H. R. Kim, K. I. Choi, K. M. Kim, I. D. Kim, G. Z. Cao and J. H. Lee, *Chem. Commun.*, 2010, **46**, 5061–5063; (b) S. J. Ding and X. W. Lou, *Nanoscale*, 2011, **3**, 3586–3588.

10 (a) X. W. Lou, L. A. Archer and Z. C. Yang, *Adv. Mater.*, 2008, **20**, 3987–4019; (b) W. Tian, C. Zhang, T. Y. Zhai, S. L. Li, X. Wang, M. Y. Liao, K. Tsukigoshi, D. Golberg and Y. Bando, *Chem. Commun.*, 2013, **49**, 3739–3741; (c) H. J. Kim, K. I. Choi, A. Q. Pan, I. D. Kim, H. R. Kim, K. M. Kim, C. W. Na, G. Z. Cao and J. H. Lee, *J. Mater. Chem.*, 2011, **21**, 6549–6555.

11 (a) Z. P. Li, Q. Q. Zhao, W. L. Fan and J. H. Zhan, *Nanoscale*, 2011, **3**, 1646–1652; (b) C. Y. Cao, W. Guo, Z. M. Cai, W. G. Song and W. Cai, *J. Mater. Chem.*, 2011, **21**, 3204–3209.

12 (a) Y. Zhao and L. Jiang, *Adv. Mater.*, 2009, **21**, 3621–3638; (b) H. C. Zeng, *J. Mater. Chem.*, 2011, **21**, 7511–7526.

13 Y. D. Liu, J. Goebl and Y. D. Yin, *Chem. Soc. Rev.*, 2013, **42**, 2610–2653.

14 X. F. Yang, J. X. Fu, C. J. Jin, J. Chen, C. L. Liang, M. M. Wu and W. Z. Zhou, *J. Am. Chem. Soc.*, 2010, **132**, 14279–14287.

15 Y. D. Yin, R. M. Rioux, C. K. Erdonmez, S. Hghes, G. A. Somorjai and A. P. Alivisatos, *Science*, 2004, **304**, 711–714.

16 X. W. Lou, Y. Wang, C. L. Yuan, J. Y. Lee and L. A. Archer, *Adv. Mater.*, 2006, **18**, 2325–2329.

17 B. Wang, J. S. Chen, H. B. Wu, Z. Y. Wang and X. W. Lou, *J. Am. Chem. Soc.*, 2011, **133**, 17146–17148.

18 W. W. Zhou, C. W. Cheng, J. P. Liu, Y. Y. Tay, J. Jiang, X. T. Jia, J. X. Zhang, H. Gong, H. H. Hng, T. Yu and H. J. Fan, *Adv. Funct. Mater.*, 2011, **21**, 2439–2445.

19 W. Wu, S. F. Zhang, F. Ren, X. H. Xiao, J. Zhou and C. Z. Jiang, *Nanoscale*, 2011, **3**, 4676–4684.

20 L. P. Zhu, N. C. Bing, D. D. Yang, Y. Yang, G. H. Liao and L. J. Wang, *CrystEngComm*, 2011, **13**, 4486–4490.

21 D. F. Zhang, L. D. Sun, C. J. Jia, Z. G. Yan, L. P. You and C. H. Yan, *J. Am. Chem. Soc.*, 2005, **127**, 13492–13493.

22 M. N. Rumyantseva, V. V. Kovalenko, A. M. Gaskov, T. Pagnier, D. Machon, J. Arbiol and J. R. Morante, *Sens. Actuators, B*, 2005, **109**, 64–74.

23 P. Sun, L. You, D. W. Wang, Y. F. Sun, J. Ma and G. Y. Lu, *Sens. Actuators, B*, 2011, **156**, 368–374.

24 P. Sun, W. N. Wang, Y. W. Liu, Y. F. Sun, J. Ma and G. Y. Lu, *Sens. Actuators, B*, 2012, **173**, 52–57.

25 D. F. Zhang, L. D. Sun, J. L. Yin and C. H. Yan, *Adv. Mater.*, 2003, **15**, 1022–1025.

26 B. L. Lv, Z. Y. Liu, H. Tian, Y. Xu, D. Wu and Y. H. Sun, *Adv. Funct. Mater.*, 2010, **20**, 3987–3996.

27 L. Vayssieres, N. Beermann, S. E. Lindquist and A. Aagfeldt, *Chem. Mater.*, 2001, **13**, 233–235.

28 Z. Z. Sun, X. M. Feng and W. H. Hou, *Nanotechnology*, 2007, **18**, 455607.

29 S. C. Naisbitt, K. F. E. Pratt, D. E. Williams and I. P. Parkin, *Sens. Actuators, B*, 2006, **114**, 969–977.

30 S. Elouali, L. G. Bloor, R. Binions, I. P. Parkin, C. J. Carmalt and J. A. Darr, *Langmuir*, 2012, **28**, 1879–1885.

31 T. Weis, R. Lipperheide and U. Wille, *J. Appl. Phys.*, 2002, **92**, 1411–1418.

32 N. Yamazoe, J. Fuchigami, M. Kishikawa and T. Seiyama, *Surf. Sci.*, 1979, **86**, 335–344.

33 M. Egashira, Y. Shimizu, Y. Takao and S. Sako, *Sens. Actuators, B*, 1996, **35**, 62–67.

34 Y. Shimizu, N. Kuwano, T. Hyodo and M. Egashira, *Sens. Actuators, B*, 2002, **83**, 195–201.